Cation Environment of $BaCeO_3$-Based Protonic Conductors: A Computational Study

Antonio Cammarata,[†,‡] Antonino Martorana,[†] and Dario Duca*[,†]

Dipartimento di Chimica Inorganica e Analitica "S. Cannizzaro" dell'Università di Palermo, Viale delle Scienze Ed. 17, I-90128 Palermo (Sicily), Italy

Received: February 5, 2009; Revised Manuscript Received: April 5, 2009

Geometry calculations were performed on pure $BaCeO_3$ fragments and on Y- and In-doped derivatives. HF and DFT approaches were used to investigate monoclinic and orthorhombic structures. The computational methods, structural models, and electronic structure investigation protocols were tuned taking into consideration and balancing the consistency of the results against the computational cost. The calculated structures and energetics parameter, as well as the detailed orbital analysis performed on the corresponding $BaCeO_3$ derivatives allowed us to explain experimental findings and to develop a procedure to study the cationic octahedral environment of doped X:$BaCeO_3$ (X = Y, In) and undoped $BaCeO_3$ protonic conductors useful to interpret experimental results and hopefully to design new experimental approaches. In detail, distances and angles of the studied materials are easily captured in the frame of the HF paradigm even by using low-level ECP basis sets. While, pure electronic-based approaches, involving the investigation of the Partial Density of States resulting from the C-Squared Population Analysis, show that the dopant species must leave unchanged, or even decrease, the local basicity of the oxygen octahedral environment in order to increase the conductivity of the $BaCeO_3$ derivatives. Whereas local structural changes that are not related to the basicity above affect to a less, if not null, extent the conductivity of the same derivatives.

Introduction

Materials with high and pure protonic conductivity are sought to improve major technological tools such as hydrogen sensors, batteries, electrolyzers, and fuel cells.[1−5] In this respect, much research effort is addressed to find and/or optimize solid oxide protonic conductors,[3,6] aiming at achieving materials with high conduction efficiency and structural/chemical stability. Among the solid oxides, perovskite-type ABO_3 materials exhibit the highest proton conductivity. Usually, the B species are tetravalent and are coordinated to six oxygen atoms in octahedral arrangements, while the A cations are located in the cavities formed by the tridimensional network of the corner-sharing octahedra. In such compounds, proton incorporation is achieved following a two-step procedure. In the first step, a given amount of tetravalent B centers are doped by trivalent species. This determines the formation of one oxygen vacancy per couple of doping cations introduced in the solid matrix. In the second step, water vapor is steamed on the doped material, so producing structural O—H groups—having acidic properties—by the following dissociative water adsorption:

$$H_2O(g) + V_O^{\bullet\bullet} + O_O^X \rightleftarrows 2OH_O^{\bullet} \quad (1)$$

Protons bound to reticular oxygen atoms are in this way introduced into the host matrix and proton diffusion is mainly driven by the phonon-assisted dynamics[7,8] of adjacent proton sharing oxygen atoms.[9,10] Accordingly, the mechanism of protonic conduction is strongly affected by local distortions interesting the proton environment and involving in particular the doped B-sites,[3] for this reason becoming of fundamental importance to the study of the local environment surrounding the doped sites.[7]

Yttrium-doped barium cerate is the reference compound for the perovskite-type proton conductors. The effect of yttrium doping followed by water absorption on the crystalline barium cerate structure has mostly been studied by neutron diffraction.[11−16] Knight attributed the structure of undoped barium cerate at room temperature to the *Pmcn* space group, with an $a^+ b^- b^-$ tilt system[17] of the CeO_6 octahedra.[16] The *Pmcn* space group was demonstrated to hold also at low yttrium doping level, while a tentative site for the proton was individuated, at the liquid helium temperature, in correspondence with a bent hydrogen located between two oxygen atoms, both belonging to the same octahedron.[18] Takeuchi et al. determined that the space group of hydrated $BaCe_{1-x}Y_xO_{3-(x)/(2)}$ remains *Pmcn* for $x < 0.1$, whereas for $x > 0.1$, the structure mostly turns to the monoclinic, *I2/m* space group.[19] In a recent neutron scattering study, Malavasi et al. confirmed that the *I2/m* space group holds for $BaCe_{0.8}Y_{0.2}O_{2.9}$, ranging from room temperature up to 773 K.[20] At higher temperatures, the crystalline structure at first shifts to orthorhombic symmetry, with space group *Imna*, then to rhombohedral and cubic symmetries, as the oxide loses the hydration water.

While most studies concern the long-range average structure, the local arrangement of perovskite-type protonic conductors was not thoroughly investigated. Only in the most recent years have X-ray absorption (XAS) studies, especially focused on dopants, investigated the environment of yttrium,[21,22] indium,[23] and gadolinium[24] in barium cerate. In particular, it was demonstrated that Y^{3+} cations induce axial distortions in the neighboring octahedral-coordinated oxygen atoms that are still effective at 750 K and are therefore related to the peculiar interaction of yttrium with the barium cerate host matrix. Kreuer pointed out that nonhomogeneity of the oxygen network can

* To whom correspondence should be addressed. E-mail: dduca@cccp.unipa.it.
† Dipartimento di Chimica Inorganica e Analitica "S. Cannizzaro" dell'Università di Palermo.
‡ Dipartimento di Scienze Fisiche e Astronomiche dell'Università di Palermo.

10.1021/jp901074p CCC: $40.75
Published on Web 05/11/2009

hinder proton mobility[3] and actually, at liquid nitrogen temperature, the XANES region of the XAS pattern is consistent with a local structure modification with respect to the dry sample that is likely associated with the preferential insertion of hydroxyl groups in the vicinity of the doped B-sites. A strong dopant−hydroxyl interaction was also observed by quasi-elastic neutron scattering experiments on Yb-doped strontium cerate.[25]

Kreuer proposed that the observed variation, by magnitude orders, of the conductivity of barium zirconate as a function of the type of the inserted dopant should be ascribed to the modification of the oxide electronic structure that influences the lattice vibrations and/or the oxide basicity. According to this point of view, a modification of the proton−oxygen chemical bond could be the predominant source of hindrance on the proton mobility.[26,27] As recently proposed by Björketun et al., a computational analysis can be useful to discriminate between the structural and electronic factors, influencing the proton mobility in the perovskite-type oxides.[28] With respect to this, several computational approaches investigated barium cerate systems[29,30] and other perovskite-like protonic conductors[31−34] by parametrized potentials for long-range and short-range interactions, while the shell model was used to simulate ionic polarization and the Mott−Littleton approach to model defects. LCAO within the Local Density Approximation (LDA) to model Kohn−Sham potential were also used,[35,36] while repulsion energies were derived from short-range potentials whose parameters were optimized on the difference between the energy band structures of the corresponding crystalline system and the energy calculated with SCF-LDA.[37] Finally, other studies[28] were mainly aimed at describing the local hydrogen properties. The works above made use of structure fragments to model local defects, corresponding to the substitution of tetravalent cations or hydroxyl groups into octahedral sites, and, in order to reproduce the crystalline structure, applied periodic boundary conditions (PBC). Supercells were also exploited to take into account dopant, defect, and proton concentration changes.

In the present work, we studied performing several geometrical optimizations of quite large fragments and using different quantum chemical (QC) approaches, $BaCeO_3$ and $Y:BaCeO_3$ clusters, which were cut starting from neutron scattering structures whose space groups belonged to the monoclinic (*I2/m*) and to the orthorhombic (*Pmcn*) systems. This procedure was followed to discriminate between the occurrence between the two space groups while, to investigate the effects of the dopant species a *Pmcn*, $In:BaCeO_3$ fragment was also taken into consideration. In particular, we tried to avoid technical procedures introducing structural artifacts. Hence, we choose to not apply QC-PBC methods in studying the local environments of structural defects because in that case, the latter could result in artificial repeats in a regular manner all over the 3D-space, probably introducing cooperative physical effects hard to be rationalized. As a consequence, a cluster approach,[38] involving suitable geometry optimization strategies, and local electronic investigations, including the Mulliken charge analysis[39−41] (*M-ca*) and the Partial Density of States (P-DOS)[42] in the frame of the C-Squared Population Analysis[43] (C-SPA), were employed.

The C-SPA approach is discussed with the model properties, the basis sets and the computational methods in the Models and Computational Details section, whereas in the Results and Discussion section it is shown that the applied protocol allows one to find a reasonable explanation of the octahedral $X:BaCeO_3$ site properties, with a good compromise between the reached computational information and the needed computational time.

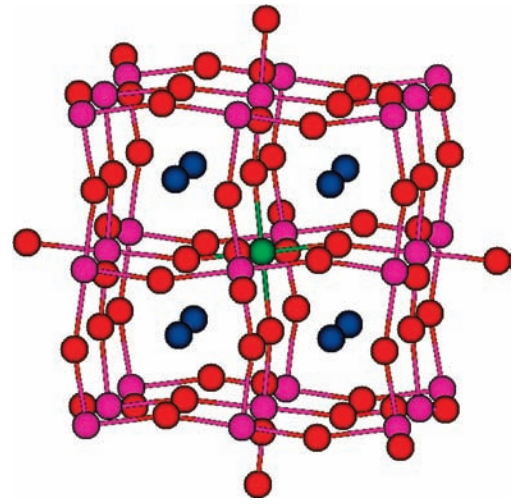

Figure 1. $\Xi:Ba_8Ce_{26}O_{62}$ fragment: Ba, Ce and O centers are in blue, purple, and red, respectively; the Ξ site (Ξ = Ce, Y, In) inside the central octahedral moiety is in green.

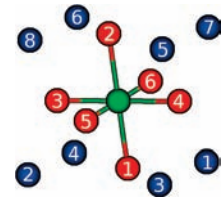

Figure 2. Details on the optimized atom moieties extracted from the larger model fragment represented in Figure 1. The central atom (Ξ = Ce, Y, In) is the zeroth one and is not explicitly pointed out, while two parallel numberings characterize Ba (1−8) and O (1−6) atoms.

Models and Computational Details

After preliminary calculations,[44] we chose the starting cluster geometries of the model systems investigated in this work, extracting them from the crystalline structures refined by neutron diffraction and belonging to the *I2/m* or *Pmcn* space groups, generally attributed to the room temperature perovskite arrangements.[18,19] In order to avoid cutoff truncation outcomes affecting the calculated properties of the B-site local environment, a large crystal fragment of suitable geometry was chosen—see Figure 1.

The symmetry of the cut assured the absence of a dipole moment on the resulting systems, while the composition of the fragment $\Xi:Ba_8Ce_{26}O_{62}$ for Ξ = Ce corresponds to a null-charged singlet-state $Ba_8Ce_{26}O_{62}$ system, attributing to the involved atoms the formal charges that they have in the crystalline structure. The doped fragments, invariably considered as hydrated and locally unprotonated, were calculated by a multiplicity equal to 1 and a resulting charge equal to −1. The latter has to be saturated in future studies, including the protonic species, to deepen the proton diffusion mechanism. A model system including two yttrium atoms, $Y_2:Ba_8Ce_{25}O_{62}$, was also considered as discussed in the section concerning the orthorhombic yttrium-doped systems. In this case, the charge was posed equal to 0 and the multiplicity to 1 while the second Y was bounded to the O labeled as 4 in Figure 2.

Along the calculations, the positions of the barium atoms and of the centers included in the ΞO_6 octahedral moiety of the starting fragment—from now on also called central octahedron—have been optimized keeping fixed to the crystalline structure coordinates,[18,19] the remaining species belonging to the external frame. An analogous partial-optimization approach was recently

applied to different solid-state systems, obtaining reliable results.[42,45,46]

Figure 2 shows the detail of the $Ba_8\Xi O_6$ moiety, hereafter called the central cluster, that was relaxed along the optimizations. As already mentioned, PBC protocols were not applied to the present study, in this way avoiding the typical ordered structural replicas characterizing the periodic applications. The average crystal structure observed by diffraction is produced by the insertion of dopants in the B-sites of barium cerate and depends on the dopant concentration. Therefore, it is assumed that in the present model, the $Ba_8\Xi O_6$ central cluster relaxes in the environment of the average structure experimentally observed, and therefore the rigid external frame brings about in an average way the interaction with the matrix.

The Gaussian03 (G03) suite of programs[47] was employed to perform the calculations in the frame of the HF and DFT paradigms.[40,41] In detail, HF and DFT B3LYP hybrid energy functional[48]—the latter inside an ONIOM environment[49]—were employed for the geometry optimizations, after the G03 standard convergence criteria. Moreover, the SCF component of the calculation was performed by a linear minimum search method, followed, if needed, by quadratic minimum search method,[50] always using the G03 standard convergence criteria. Unless expressly stated, the multiplicity of the systems was fixed to 1—i.e., closed shell systems were mostly considered.

In the calculations of the geometric and energetic properties of the Ξ:$Ba_8Ce_{26}O_{62}$ fragments, the O atoms belonging to the central octahedron and the external cage—see Figures 1 and 2—were described by the 6-31+G(d,p)[51] and 3-21G[52] basis set, respectively. The SBKJC VDZ ECP[53] pseudopotential was used for the Ce atoms. The SBKJC VDZ ECP and the CRENBL ECP[54] pseudopotentials were used separately in different optimizations for the Ba atoms, while the SBKJC VDZ ECP (Ξ = Y, In) basis sets, if not otherwise specified, were employed to describe the central Ξ atoms. The Stuttgart RSC 1997 ECP[55] (Ξ = Y) and the aug-cc-pV5Z-PP[56] (Ξ = In) pseudopotentials were also applied. Different pseudopotentials for the same centers were used, as detailed in the following Results and Discussion section, along different geometry optimizations in order to test their suitability in studying the title materials. An orbital analysis was also performed on the calculated $BaCeO_3$ derivatives through the inspection of Partial DOS (P-DOS). The latter was performed considering the orbital population as obtained by the C-SPA[43] procedure, using an homemade code. In this, applying the Linear Combination of Atomic Orbitals (LCAO) approximation, the molecular orbital (MO) ϕ_i, relative to the eigenvalue ε_i of a given system, is defined as follows:

$$\phi_i = \sum_j c_{ji}\chi_j \tag{1a}$$

where χ_j is the j^{th} atomic orbital (AO) into the involved system and c_{ji} is the coefficient of χ_j in the ϕ_i linear combination. The contribution, $\rho_{\alpha,i}$, of the α^{th} AO to the ϕ_i MO can be defined as:

$$\rho_{\alpha,i} = c^2_{\alpha,i}\left(\sum_j c^2_{ji}\right)^{-1} \tag{2}$$

while the contribution to the same MO of a given cluster of atoms A is given by:

$$\rho_{A,i} = \sum_{\alpha\in A} c^2_{\alpha i}\left(\sum_j c^2_{ji}\right)^{-1} \tag{3}$$

Equations 2 and 3 allow one to isolate and compare the electronic contributions to single molecular orbitals or to molecular orbital arrangements corresponding to a given bin ($\Delta\varepsilon_i$), fixing the discrete energy units in the DOS analysis. A continuous function $\rho(\varepsilon)$ is achieved by convolution of fixed-width Lorentzian functions weighted by $\rho_{A,i}$ and centered on ε_i.

Results and Discussion

To the best of our knowledge, computational approaches to the perovskite derivatives presently reported in literature have employed parametrized potentials,[29,30,32,33,35] usually obtained by fits of diffraction results relative to reference materials. These potentials allowed one to calculate properties of systems as large as hundreds of atoms, but are somewhat constrained by their developmental procedures, possibly driving the structure optimizations to forced geometry minima. On the contrary, the here-proposed approach, mainly relying on ab initio HF methods, should give locally unconstrained results[41] on the central cluster, although it introduces structural and electronic constraints on the surrounding fixed framework. As we will show, the considered fragment is, however, large enough and these border restrictions are not affecting the local properties of the central $Ba_8\Xi O_6$ moiety.

In this section, the arguments are separated considering the different composition and symmetry, which characterize the Ξ_n:$Ba_8Ce_{27-n}O_{62}$ fragments (Ξ = Ce, Y, In). At first, the monoclinic framework is analyzed for the undoped and the yttrium-doped systems, employing different basis sets for the Ba and the Ξ atoms. Then, the orthorhombic framework is considered, distinguishing among the undoped, yttrium-doped, and indium-doped systems. For the orthorhombic systems, beside the check of different basis sets, the C-SPA/P-DOS analysis and the *M-ca* procedure are also outlined.

Monoclinic Framework. The average structure of hydrated $BaCe_{1-x}Y_xO_{3-(x)/(2)}$—with $0.15 < x < 0.25$—is mostly arranged in the *I2/m* monoclinic space group.[19] The atomic positions, as determined by refining the neutron powder diffraction (NPD) data taken at room-temperature in the *I2/m* space group,[19] were considered in order to study the Y- and Ce- centered clusters.

Ce-Centered Cluster in the Monoclinic Framework. In the geometry optimization, the Ce atom inside the central octahedron was treated by the SBKJC VDZ ECP basis set—supplying for the cerium atom 12 valence electrons—while the Ba atoms were treated both by the SBKJC VDZ ECP and CRENBL ECP basis sets. Relevant relaxed distance and angle values are reported in the last two columns of Table 1; while the corresponding experimental findings relative to NPD and EXAFS, respectively, are summarized in the first two. The experimental values determined at room-temperature by NPD analysis were used as starting input in the SBKJC and CRENBL optimizations. The "refined" $|\Delta E|$, calculated as the difference between the energy of the optimized geometry and the energy of the geometry corresponding to the starting NPD structures,[19] determined at the same calculation level, resulted comparable for the SBKJC and the CRENBL optimization, being ΔE equal to −0.03 and −0.04 au, respectively.

The sets of oxygen atoms {5,1,6,2}, {4,6,3,5}, and {3,1,4,2} single out three different planes, crossing at the central cerium atom, both before and after the calculations and irrespective of the basis set employed in the latter. In each of these planes, two couples of oxygen atoms, together with the cerium atom, individuate two incident lines, making two opposite-to-the-vertex pair of angles. Taking into account that no constraints are imposed on the optimized atomic coordinates, this result demonstrates that the atomic arrangement of the central cluster fits into the average long-range structure determined by dif-

TABLE 1: Relevant Geometrical Parameters Characterizing the Central Octahedron Environment of the Undoped Monoclinic, *I2/m* $BaCeO_3$, Fragment

distances[a]/pm	NPD[b]	EXAFS[c]	SBKJC[d]	CRENBL[d]
d_{Ce-O1}	225		230	230
d_{Ce-O2}	225		230	230
d_{Ce-O3}	223		224	218
d_{Ce-O4}	223		224	218
d_{Ce-O5}	225		226	220
d_{Ce-O6}	225		226	220
$<d_{Ce-O}>$	224	227	227	223
d_{Ce-Ba1}	389		395	384
d_{Ce-Ba2}	373		394	381
d_{Ce-Ba3}	382		377	369
d_{Ce-Ba4}	379		376	370
d_{Ce-Ba5}	379		376	370
d_{Ce-Ba6}	382		377	369
d_{Ce-Ba7}	373		394	381
d_{Ce-Ba8}	389		395	384
$<d_{Ce-Ba}>$	381	381	386	376
angles/(deg)	NPD	EXAFS	SBKJC	CRENBL
$a_{O1-Ce-O5}$	89.1		89.1	89.1
$a_{O2-Ce-O3}$	89.6		88.7	88.4
$a_{O3-Ce-O5}$	91.9		91.3	90.6

[a] For the atomic labeling see Figure 2. [b] Neutron powder diffraction parameter values as determined at room-temperature by Takeuchi et al.[19] These geometrical parameters were also used as starting input in the optimizations whose results are summarized in the SBKJC and CRENBL columns. [c] Results at liquid nitrogen temperature reported by Giannici et al.[22] [d] The SBKJC and CRENBL labels refer to the SBKJC VDZ ECP and CRENBL ECP basis sets used for the Ba atoms, respectively. The basis sets of the other atoms were maintained constant in the calculations—see Models and Computational Details section.

TABLE 2: Relevant Geometrical Parameters Characterizing the Central Octahedron Environment of the Yttrium-Doped Monoclinic, *I2/m* Y:$BaCeO_3$, Fragment

distances[a]/pm	NPD[b]	EXAFS[c]	SBKJC[d]	CRENBL[d]
d_{Y-O1}	225		235	229
d_{Y-O2}	225		235	229
d_{Y-O3}	223		229	225
d_{Y-O4}	223		229	225
d_{Y-O5}	225		231	229
d_{Y-O6}	225		231	229
$<d_{Y-O}>$	224	226	231	227
d_{Y-Ba1}	389		388	379
d_{Y-Ba2}	373		386	376
d_{Y-Ba3}	382		366	369
d_{Y-Ba4}	379		366	371
d_{Y-Ba5}	379		366	371
d_{Y-Ba6}	382		366	369
d_{Y-Ba7}	373		386	376
d_{Y-Ba8}	389		388	379
$<d_{Y-Ba}>$	381	377	377	374
angles/(deg)	NPD	EXAFS	SBKJC	CRENBL
$a_{O1-Y-O5}$	89.1		89.5	89.9
$a_{O2-Y-O3}$	89.6		89.0	89.3
$a_{O3-Y-O5}$	91.9		90.8	91.4

[a] For the atomic labeling see Figure 2. [b] Neutron powder diffraction parameter values as determined at room-temperature by Takeuchi et al.[19] These geometrical parameters were also used as starting input in the optimizations whose results are summarized in the SBKJC and CRENBL columns. [c] Results at 120 K reported by Longo et al.[21] The Y—O distance reported is the average of two Y—O lengths: 2-fold at 233 pm and 6-fold at 223 pm. [d] The SBKJC and CRENBL labels refer to the SBKJC VDZ ECP and CRENBL ECP basis sets used for the Ba atoms, respectively. The basis sets of the other atoms were maintained constant in the calculations—see Models and Computational Details section.

fraction without large local distortion. A similar result holds true also for the Ce—Ba interactions. However, in contrast with the diffraction analysis, the structure relaxation following the optimization introduces an axial distortion in the CeO_6 octahedron. Finally, the SBKJC VDZ ECP and the CRENBL ECP, which for the barium atoms respectively provide 2 and 10 valence electrons, show quite similar results, although the latter seems to accentuate the axial distortion around the oxygen octahedral site.

Y-Doped Cluster in the Monoclinic Framework. To study the modifications induced into the structure by substituting the octahedral cation, we performed a geometrical optimization by considering the same basis set used in the preceding section, substituting the inner Ce atom of the central octahedron with one Y atom. The starting geometry was the same as in the previous calculation. With respect to this point, it must to be stressed that the NPD crystallographic analysis cannot distinguish yttrium and cerium, being just able to point out—by using information on the relative atomic abundance characterizing the involved material—the average positions of the cations that occupy the octahedral sites.[19]

As for the undoped system, two geometrical optimizations of the same structure were performed, using the SBKJC VDZ ECP and CRENBL ECP basis sets to describe the Ba atoms. Relevant distances and angles concerning the monoclinic Y:$Ba_8Ce_{26}O_{62}$ fragment are reported in Table 2. The relaxation of the experimental structures, occurring by the optimizations, produced changes in the distance values below 5%, while the changes in the angle values were limited to the 2%. The refined $|\Delta E|$ value was larger for the SBKJC than for the CRENBL optimization, being the ΔE values equal to −0.12 au for the former and −0.05 au for the latter. Hence, for the monoclinic systems, the refined $|\Delta E|$ behavior is not systematic with respect to the level of the considered basis set.

The interesting geometrical properties already observed for the undoped systems, regarding the pair of opposite a_{O-Y-O} angles and the d_{Y-O} and d_{Y-Ba} distances, involving the atoms of the central octahedron moiety, were still holding in the Y:$Ba_8Ce_{26}O_{62}$ doped fragment. However, the octahedral axial distortion in the latter resulted a little smaller than the one obtained in the calculation of the undoped models site and therefore the computational outcome does not agree with the EXAFS result that determined the presence of two Y—O first-neighbor distances, independently of the Y concentration.

Orthorhombic Framework

Ce-Centered Cluster in the Orthorhombic Framework. Undoped barium cerate was attributed to the *Pmcn* (*Pnma*, in standard notation) space group, by neutron diffraction taken at liquid helium temperature.[18] To study the system above, the central octahedron of Figure 2 was included in a *Pmcn* rigid cage, thus obtaining the starting structure qualitatively represented in Figure 1.

As in the preceding sections, the SBKJC and CRENBL optimizations were performed—for details on the basis set and pseudopotential employed in the calculations, see Table 3. Moreover, to take account of correlation effects, without increasing the computational cost, a third geometrical optimization was performed, following ONIOM prescriptions. In this, the $Ba_8Ce_{27}O_{62}$ fragment was fractioned in two layers: the Ba_8CeO_6 and the $Ce_{26}O_{56}$ fragments. The former (model system),

TABLE 3: Relevant Geometrical Parameters Characterizing the Central Octahedron Environment of the Undoped Orthorhombic, *Pmcn* $BaCeO_3$, Fragment

distances[a]/pm	NPD[b]	EXAFS[c]	SBKJC[d]	CRENBL[d]	ONIOM[e]
d_{Ce-O1}	225		227	224	226
d_{Ce-O2}	225		227	224	226
d_{Ce-O3}	224		228	224	228
d_{Ce-O4}	224		228	224	228
d_{Ce-O5}	225		228	224	228
d_{Ce-O6}	225		228	224	228
$<d_{Ce-O}>$	225	227	228	224	227
d_{Ce-Ba1}	391		380	383	387
d_{Ce-Ba2}	377		400	387	404
d_{Ce-Ba3}	369		374	368	385
d_{Ce-Ba4}	384		383	378	390
d_{Ce-Ba5}	384		383	378	390
d_{Ce-Ba6}	369		374	368	385
d_{Ce-Ba7}	377		400	387	404
d_{Ce-Ba8}	391		380	383	387
$<d_{Ce-Ba}>$	380	381	384	379	392
angles/(deg)	NPD	EXAFS	SBKJC	CRENBL	ONIOM
$a_{O1-Ce-O5}$	89.0		91.3	90.1	92.0
$a_{O2-Ce-O3}$	91.6		89.7	90.8	91.2
$a_{O3-Ce-O5}$	90.4		90.5	91.4	90.0

[a] For the atomic labeling see 2. [b] Neutron powder diffraction parameter values as determined at liquid helium temperature by Knight.[18] These geometrical parameters were also used as starting input in the optimizations whose results are summarized in the SBKJC, CRENBL, and ONIOM columns. [c] Results at liquid nitrogen temperature reported by Giannici et al.[22] [d] The SBKJC and CRENBL labels refer to the SBKJC VDZ ECP and CRENBL ECP basis sets used for the Ba atoms, respectively. The basis sets of the other atoms were maintained constant in the calculations—see Models and Computational Details section. [e] In the ONIOM calculation the optimized Ba_8CeO_6 model system, including the central octahedron, was treated at B3LYP level while the remaining $Ce_{26}O_{56}$ real system was treated at HF level, the basis sets used were the same used in the SBKJC optimization.

corresponding to the central octahedron environment, was treated at B3LYP level while the latter (real system), surrounding the central octahedron environment, was treated at HF level. The basis sets used were the ones employed in the SBKJC treatment.

For the *Pmcn* $BaCeO_3$ fragment system, the refined $|\Delta E|$ value was smaller in the SBKJC than in the CRENBL approach, being ΔE for the former −0.02 au and for the latter −0.08 au. Table 3 shows relevant experimental and calculated orthorhombic barium cerate distances and angles. Beside few overestimated ONIOM and SBKJC distances and in addition the ONIOM $<d_{Ce-Ba}>$ average value, it is clear that the calculated Ce—O and Ce—Ba distances as well as the O—Ce—O angles are in agreement with the corresponding NPD[18] and EXAFS results.[22]

As for the monoclinic systems, it is here remarked that the pairs of angles and distances opposite to the Ce vertex in the CeO_6 octahedron remains in pairs equal in the relaxed structure, like it is imposed by the *Pmcn* symmetry. This property is observed also within the less fitting SBKJC and ONIOM approaches while, straightforwardly, the CRENBL calculation well reproduces the whole experimental findings. Other comparisons with calculated results finally show good agreement with the Ce—O distance found for an orthorhombic structure by Glockner et al.[29] (225 pm) and an understandable disagreement with the same Ce—O distance found by Glockner et al.,[29] Wu et al.[30] and Munch et al.[35] for cubic structures (220 ÷ 221 pm).

Y-Doped Cluster in the Orthorhombic Framework. Also in this case, the central octahedron fragment was optimized considering two different basis sets for the Ba atoms: SBKJC and CRENBL model systems. The refined $|\Delta E|$ value is smaller for the SBKJC than for the CRENBL optimization, being ΔE for the former −0.04 au and for the latter −0.10 au. Besides the SBKJC VDZ ECP used for both of the above systems, the Y atom was also described by the Stuttgart RSC 1997 ECP basis set when the CRENBL parametrization was used for the Ba atom: CS1, CS2, and CS3 model systems.

Although the SBKJC and the Stuttgart basis sets include for the yttrium atom the same number, i.e. 11, of valence electrons the latter involves a larger number of Gaussian functions, accounting for diffuse and polarization effects, which for this and for taking into consideration also relativistic effects give a more accurate description of the electronic properties.

Therefore, by using CS1, we intended to investigate the effect of a higher level basis set on the inner atom of the central octahedron. Both the charge and multiplicity state of the fragment were unchanged in the CS1 system with respect to those employed in the SBKJC and CRENBL approaches. Conversely, by the CS2 approach, we investigated the effect of the change of the system multiplicity state, imposing the triplet-state to the $Y:Ba_8Ce_{26}O_{62}$ doped fragment. Finally, by the CS3 approach, we analyzed the effects of a larger atom cluster optimization, including in the latter the Ce atoms directly linked to the O atoms of the central octahedron—see Figures 1 and 2. In order to analyze the Y-doped system, we also considered a bisubstituted fragment: $Y2:Ba_8Ce_{25}O_{62}$, which was treated by the CS1 approach, managing the second Y atom even by the more performing Stuttgart RSC 1997 ECP basis set. This system was labeled Y-2.

The starting geometry used to calculate the $Y:BaCeO_3$ derivatives was the NPD one already used for the orthorhombic $BaCeO_3$ derivative. Relevant distances and angles of the *Pmcn* $Y:BaCeO_3$ fragments and related experimental findings are reported in Table 4. The introduction of the higher level basis set used for the Y atom in the CS1 approach did not carried significant variation on the optimized geometrical parameter values while on the whole, computational (SBKJC, CRENBL, CS1) and experimental results revealed a satisfying agreement—see Table 2 for the NPD values.

The agreement is obtained although the model disregards some inferences, originating by the EXAFS analysis.[21] The latter have indeed suggested that, due to the introduction of dopant species in the $BaCeO_3$ derivatives, structural vacancy defects, not considered in the model, may occur. It is interesting to notice that both the experimental and the computational results agree in pointing out a slight contraction of the barium shell toward the yttrium species. This is likely due to the reduced positive charge characterizing the doped site—see Electronic Population Analysis section. The CS2 column of Table 4 reports the geometrical parameters found, performing the fragment calculation at the triplet-state.

In this case, the Y—O distances does not differ from those obtained when a closed-shell system is taken into consideration, while the Y—Ba distances are split in two groups formed by six and two distances of ∼380 and 355 pm, respectively. The two sets of Y—O distances observed by EXAFS[21] and attributed to an axial elongation of the YO_6 octahedron, were not reproduced by the computational approaches. The length inhomogeneity could be experimentally produced by the structural vacancy defects above and/or by other local distortion that were not taken into consideration by the models so far described. The disagreement is indeed intriguing, being the Y—O distance inhomogeneity present at temperatures as high as 773 K, also

TABLE 4: Relevant Geometrical Parameters Characterizing the Central Octahedron Environment of the Yttrium-Doped Orthorhombic, *Pmcn* Y:$BaCeO_3$, Fragment

distances[a]/pm	EXAFS[b]	SBKJC[c]	CRENBL[c]	CS1[d]	CS2[d]	CS3[d]	Y-2[e]
d_{Y-O1}		232	228	228	228	225	226
d_{Y-O2}		232	228	228	228	225	228
d_{Y-O3}		231	227	227	228	225	220
d_{Y-O4}		231	227	227	228	225	237
d_{Y-O5}		233	228	228	227	226	228
d_{Y-O6}		233	228	228	227	226	230
$<d_{Y-O}>$	226	232	228	228	228	225	228
d_{Y-Ba1}		372	377	377	381	364	356
d_{Y-Ba2}		391	380	380	380	367	387
d_{Y-Ba3}		367	362	362	355	347	356
d_{Y-Ba4}		375	373	372	376	362	378
d_{Y-Ba5}		375	373	372	376	362	355
d_{Y-Ba6}		367	362	362	355	347	363
d_{Y-Ba7}		391	380	380	380	367	381
d_{Y-Ba8}		372	377	377	381	364	382
$<d_{Y-Ba}>$	376	376	373	373	373	360	370
angles/(deg)	EXAFS	SBKJC	CRENBL	CS1	CS2	CS3	Y-2
$a_{O1-Y-O5}$		88.9	89.9	89.9	89.3	91.6	90.5
$a_{O2-Y-O3}$		89.5	89.1	90.9	90.4	89.3	92.5
$a_{O3-Y-O5}$		90.3	90.9	90.9	91.3	91.6	95.1

[a] For the atomic labeling see Figure 2. [b] Results at 120 K reported by Longo et al.[21] [c] The SBKJC and CRENBL labels refer to the SBKJC VDZ ECP and CRENBL ECP basis sets employed for the Ba atoms, respectively. The basis sets of the other atoms were maintained constant in the different calculations and equal to those employed for the homonym monoclinic systems. [d] In the CSn calculations the Y atom was treated by the Stuttgart RSC 1997 ECP basis set: in the CS1 and CS2 calculations closed-shell singlet-state and open-shell triplet-state systems were considered while in the CS3, closed-shell, calculation the Ce atoms linked to the O atoms of the central octahedron were also relaxed. [e] The Y2:$Ba_8Ce_{25}O_{62}$ system was treated as the mono substituted CRENBL Y:$Ba_8Ce_{26}O_{62}$ one. The second yttrium atom is linked to the first one through the O4 atom.

under very different hydration conditions.[21] It is finally interesting to observe that the relaxation of a larger atom cluster (Y:$Ba_8Ce_6O_6$ instead of Y:Ba_8O_6), taken into consideration by the CS3 approach, did not increase the reliability of the optimization performance, managing the Y:$Ba_8Ce_{26}O_{62}$ fragment. This result is however not surprising and already it was observed, computationally treating large fragment of zeolite materials.[49] In the calculation so far considered, it can be observed the same geometrical properties, characterizing pairs of angles and distances opposite to the Y atom inside the central octahedron. However, in this case, the axial distortion is smaller than that shown by the related monoclinic system.

The Y-2 model was investigated in order to find a possible origin of the bimodal distribution pointed out by the EXAFS results,[21] which were not reproduced hitherto by any of the considered models. For this, considering the structure optimized by the CS1 approach, at first we performed a preliminary calculation in which the position of the second yttrium (introduced by substitution of the Ce atom linked to O4) and its octahedral oxygen environment were allowed to optimize then, starting from the locally rebalanced structure, the central octahedron and the barium atoms were relaxed as usual. By this *naive* procedure, the sets of oxygen planes {5,1,6,2}, {4,6,3,5}, {3,1,4,2}, and the characteristic symmetry around the yttrium inside the central octahedron were as expected lost.

Analyzing the results on the Y-2 system above and being aware of the limits of the procedure followed, it is possible to attempt a rationalization of the Y—O bimodal distance set—around 233 and 223 pm, with weight (2)/(3) and (1)/(3), respectively—determined by the EXAFS approaches applied to Y:$BaCeO_3$ derivatives.[21] In fact, three characteristic Y—O distances, having different statistical weights, can be recognized in the column Y-2 of Table 4; that is ~220, 230, and 240 pm, being the longest and the shortest distance on the same line including the two Y atoms present in the Y2:$Ba_8Ce_{25}O_{62}$ fragment. Considering the longest and shortest distances as constituting two different groups of offset-points in the d_{Y-O} main-distance-set (with value around 230 pm), we could infer that an input to the experimental Y—O distance distribution could be given by a bimodal spread on the main-distance-set, originated by the clustering of the Y—O—Y local arrangements.

Concerning this, it can be argued that the Y—O—Y configuration includes a larger number of Ba atoms in the average Y coordination shell, with respect to that of the Y—O—Ce configuration. Since the Debye—Waller factor can be regarded as a parameter measuring the static disorder around a scattering center, the hypothesis that the local disorder, caused by the Y clustering, could generate the apparent bimodal Y—O distribution is also supported by the higher Debye—Waller factor value experimentally found (in the doped system) for the Y—Ba coordination shell,[21] with respect of that found (in the undoped system) for the Ce—Ba coordination shell.[22]

In-Doped Cluster in the Orthorhombic Framework. In contrast with yttrium, that has a solubility limit of ~15% of the available B sites of $BaCeO_3$, indium can be inserted into the barium cerate matrix in any amount, producing eventually a change in the symmetry of the In:$BaCeO_3$ mixed oxide. At low indium concentration, the doped oxide is still orthorhombic, with space group *Pmcn*.

Calculations on one *Pmcn* In:$Ba_8Ce_{26}O_{62}$ fragment were performed in order to investigate the peculiar behavior of indium hence to compare the electronic properties of yttrium and indium doped derivatives. Barium cerate In-doped, In:$BaCeO_3$, materials show indeed important differences with respect to the Y-doped derivatives, driving as an example the formation of very regular oxygen and barium neighboring shells and entering in the host oxide in any amount.[23]

Relevant distances and angles of the *Pmcn* In:$BaCeO_3$ fragment and corresponding experimental findings are reported in Table 5. The CRENBL approach, although showing average distance values consistent with the experimental ones, in disagreement with the EXAFS results, shows that both the In—O and In—Ba distances should be characterized by specific distributions. The anomalous behavior between experimental and calculated In—O findings is clearly removed increasing the level of the In basis set: aug-cc-pV5Z-PP, employed in the CVP approach. In fact, the aug-cc-pV5Z-PP, as the SBKJC ECP basis set, both provide 21 valence electrons and take account for relativistic effects. But, at variance with the latter, the former, which is a correlation-consistent basis set usually employed in the highest level calculations, includes a very larger number of diffuse and polarization basis functions.

Like for the other calculated doped and undoped systems, the geometrical features concerning pairs of angles and distances opposite to the In atom inside the central octahedron still hold, when the aug-cc-pV5Z-PP are employed. Finally, it is here recalled that the calculations on Y- and In-doped systems are able to capture an important property recently shown by EXAFS on doped $BaCeO_3$ derivatives[23] and pointing out the larger shrinking of the octahedral oxygens and the surrounding barium atoms on the indium respecting the yttrium atom.

Electronic Population Analysis. In order to deepen our insight into the electronic characteristics of the $Ba_8\Xi O_6$ moiety,

TABLE 5: Relevant Geometrical Parameters Characterizing the Central Octahedron Environment of the Indium-Doped Orthorhombic, *Pmcn* In:$BaCeO_3$, Fragment

distances[a]/pm	EXAFS[b]	CRENBL[c]	CVP[d]
d_{In-O1}		213	220
d_{In-O2}		213	220
d_{In-O3}		223	220
d_{In-O4}		223	220
d_{In-O5}		226	222
d_{In-O6}		226	222
$<d_{In-O}>$	216	221	221
d_{In-Ba1}		368	370
d_{In-Ba2}		375	375
d_{In-Ba3}		352	353
d_{In-Ba4}		367	367
d_{In-Ba5}		367	367
d_{In-Ba6}		352	353
d_{In-Ba7}		375	375
d_{In-Ba8}		368	370
$<d_{In-Ba}>$	364	365	366
angles/(deg)	EXAFS	CRENBL	CVP
$a_{O1-Y-O5}$		89.9	90.1
$a_{O2-Y-O3}$		90.6	89.7
$a_{O3-Y-O5}$		90.7	89.9

[a] For the atomic labeling see Figure 2. [b] Results at liquid nitrogen temperature reported by Giannici et al.[23] [c] The CRENBL labels refer to the homonym basis set employed for the Ba atoms. The basis sets of the other atoms are equal to those already employed in the CRENBL approaches and are described in the Models and Computational Details section. [d] In the CVP calculation the In atom was treated by the aug-cc-pV5Z-PP basis set as reported in https://bse.pnl.gov/bse/portal.[57]

hence to shed light on the effects of the dopant species on the corresponding local electronic properties, we applied C-SPA/P-DOS analysis and *M-ca* approach on the *Pmcn* Ξ:$Ba_8Ce_{26}O_{62}$ structures, on systems treated at the same level of calculation, namely the CRENBL one, in the hypothesis that local electronic changes could be related to changes in the protonic conduction properties. The C-SPA/P-DOS procedure was carried out on the fragment cut corresponding to the orthorhombic structure because it is characteristic of low-doped compounds and then can be suitable for the analysis of the noninteracting dopant sites considered in the present work. The Ξ:$Ba_8Ce_{26}O_{62}$ fragment was clustered to form four sets of atomic species to be simultaneously analyzed: (i) the $Ba_8ΞO_6$ moiety (ii) the Ba_8 atomic cluster, (iii) the Ξ species, and (iv) the O_6 atomic cluster of the central octahedron. The ρ *vs*. ε curves of these atomic groups are reported in Figure 3 with the bar representation of the Ξ:$Ba_8Ce_{26}O_{62}$ fragment eigenstates. The ρ curves represent the orbital contribution of a given atomic set, among those considered, to the MOs characterizing the $Ba_8ΞO_6$ central moiety, while the abscissa ε fits the energy range considered.

An energy range, close to the HOMO region and interesting the $Ba_8ΞO_6$ central moiety of the Ξ:$Ba_8Ce_{26}O_{62}$ fragment, is in the following analyzed. At first, it should be noticed that, in the considered energy limits, the eigenvalue ranges of the whole Ξ:$Ba_8Ce_{26}O_{62}$ fragment, singularly individuated by the red bars, are roughly coincident with the P-DOS peak widths of the selected atomic sets belonging to the $Ba_8ΞO_6$ moiety. Moreover, the presence of two characteristic peaks can at first be observed in Figure 3. These are centered at ca. − 38.0 and − 19.0 eV and correspond to MOs almost entirely constructed with the Ba_8 atomic orbitals, independently of the Ξ cation.

Concerning the Y-doped system, it can be noticed that the yttrium together with the barium and oxygen AOs are the main

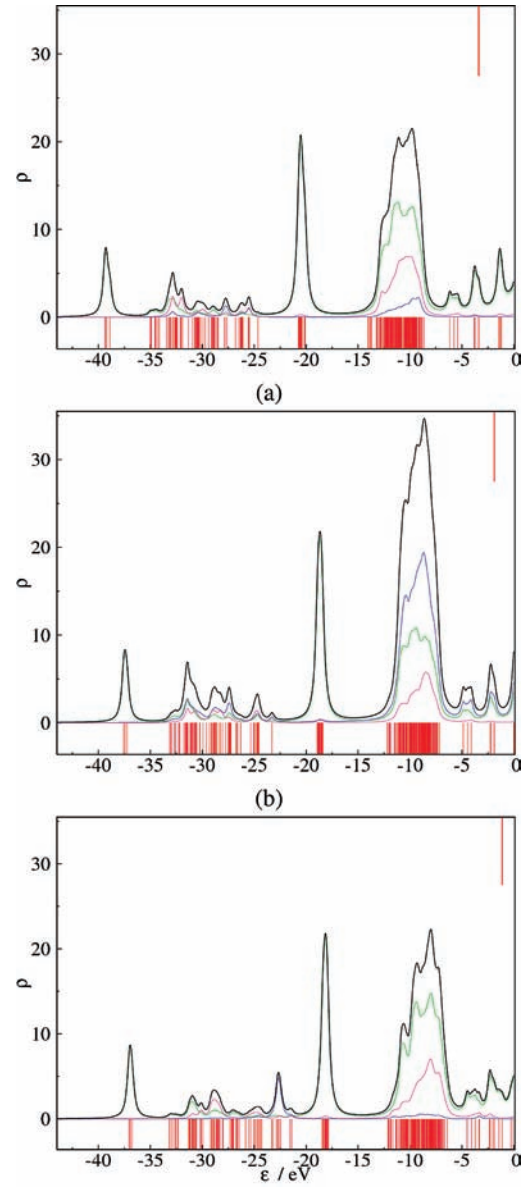

Figure 3. C-SPA/P-DOS analysis of the Ξ:$Ba_8Ce_{26}O_{62}$ fragment treated by the CRENBL approach: orbital contribution of atomic sets, included in the $Ba_8ΞO_6$ central cluster (Ba_8 group: green line; Ξ atom: blue line; O_6 group: purple line; $Ba_8ΞO_6$ moiety: black line), to the $Ba_8ΞO_6$ MOs against energy values, ρ *vs*. ε: (a) undoped, (b) Y-doped, (c) In-doped *Pmcn* systems. The red bars individuate the *i* eigenstates of the whole Ξ:$Ba_8Ce_{26}O_{62}$ fragment. The ρ lines are obtained by a convolution of fixed-width Lorentzian curves centered on the energy bin used in the DOS analysis, being the height proportional to the weight of the AO set contribution in the bin. The red line on the top shows the border between HOMO and LUMO.

contributors to the MOs corresponding to the eigenvalues in the range from −15.0 to −6.0 eV. Conversely, in the undoped systems, the cerium atom of the central octahedron clearly gives a smaller contribution to the MOs in this energy range as well as in the remaining range here analyzed. Interestingly, the MOs related to the eigenvalues in the range starting from ∼−6.0 eV up to the HOMO region are entirely attributable to the barium AOs in the undoped systems, while in the Y-doped system, the same MOs seem to be produced by a mixing of barium and yttrium AOs. The CRENBL C-SPA/P-DOS plot of the In-doped system seems to strictly resemble that of the undoped system, being however the indium AO contribution mainly centered at

TABLE 6: Mulliken Charges Determined by the CRENBL Approach for Relevant Centers of the Ξ:$Ba_8Ce_{26}O_{62}$ Fragments

center[a]	Mulliken charge/au. Ξ = Ce	Ξ = Y	Ξ = In
Ba1	−0.3	0.0	−0.15
Ba2	0.4	0.6	0.4
Ba3	0.10	0.4	0.2
Ba4	−0.14	0.15	−0.16
Ba5	−0.14	0.15	−0.16
Ba6	0.10	0.4	0.2
Ba7	0.4	0.6	0.4
Ba8	−0.3	0.0	−0.14
Ξ	2.8	−1.3	2.5
O1	−1.4	−1.3	−1.5
O2	−1.4	−1.3	−1.5
O3	−1.4	−1.3	−1.5
O4	−1.4	−1.3	−1.5
O5	−1.4	−1.3	−1.5
O6	−1.4	−1.3	−1.5
<O>[b]	−0.8	−0.8	−0.8

[a] For the atom numbering, see Figure 2. [b] The average value was taken on the charges of the saturated nonoctahedral oxygens; the standard deviation is constant (±0.1), irrespective of Ξ.

∼− 22.7 eV, where the MOs seem to be entirely determined by the same indium AOs.

Moreover, the substitution of cerium with yttrium atoms seems to localize a negative charge on the doped sites.[21] Following the *M-ca* procedure, this characteristic is plainly captured by our calculations, which show a decrease (toward negative values) of the Mulliken charge on the Y-substituted site by ∼− 4.1 au, referring to the CRENBL results, see Table 6. Interestingly, this strong effect is not observed for the In-doped fragment, which conversely is characterized by a very smaller change of the charge (−0.3 au) on the indium site in respect of the undoped one.

Therefore, with the caution that has to be deserved in considering and comparing Mulliken charges, we can infer a substantially different local behavior of In-doped and Y-doped materials. The speculation above is supported by the observation that all of the saturated oxygens, except the octahedral ones, have very similar Mulliken charge (on the average − 0.8 ± 0.1 au), irrespective of the Ξ:$Ba_8Ce_{26}O_{62}$ fragment considered; while the Mulliken charge of the oxygens on the central octahedron has a characteristic and constant behavior oppositely related to that of the charge of the central atom inside it. The average charge difference on the oxygens surrounding yttrium and indium, taking the average charge of the oxygens neighboring cerium as zero, is indeed ∼0.1 and −0.1 au,[58] see Table 6. These findings are in agreement with a higher local basicity of the ΞO_6 moiety, in the case of In with respect to Y derivatives. Finally, it is observed in passing that the Mulliken charge distribution on the Ba atoms is more scattered than that on the O atoms.

The analysis on the Mulliken charges above and the inspection of Figure 3 allow us to explain the larger miscibility and the lower conductivity of indium respecting yttrium atoms in the $BaCeO_3$ perovskite structures.[21,23] Concerning the miscibility, it can be argued that indium, although inducing local shrinking distortions, caused by its smaller size, could be introduced in the $BaCeO_3$ materials in any amount since its AOs seem to behave like those of the Ce atom—see the Ce and In contribution to the large peak around −10 eV in Figure 3. An opposite behavior is conversely shown by the yttrium center that strongly interacts with the neighboring oxygen and barium atoms and induces local isotropic expansion of the surrounding octahedron environment: d_{Y-O} = 233 pm—see note b of Table 4. This could contribute to the experimentally observed structural instability, producing unmixing phenomena—see below—in the Y:$BaCeO_3$ compounds.[22]

With respect to the conductivity, it can be inferred that the contraction of the central octahedron, namely of the octahedron including the dopant, observed in the case of the In:$BaCeO_3$ derivatives should cause a reduced ability in the proton transport, occurring by interoctahedral proton relocations.[33] This fact coupled with the higher electron charge, determined by *M-ca*, on the oxygens surrounding the indium atom in respect to the yttrium one, easily could explain the reduced conductivity of the In-doped materials,[21,23] since the smaller doped octahedron should have limited exchange capability with neighboring octahedrons (even more limited if the latter were also doped and as a consequence smaller) while the higher negative charge should even increase the resistance of the proton diffusion from the same In-doped octahedrons. Moreover, a proton moving from one oxygen of the latter to one of an undoped octahedron has to overcome an unfavorable charge gradient—protons have actually to move toward more positive sites—at variance with the event involved in the proton displacement from the oxygens of the Y-doped to the oxygens of the undoped octahedrons. This is in agreement with the interpretation proposed by Kreuer,[3] which directly relates the conductivity of a doped $BaCeO_3$ material to the basicity variations of the oxygen octahedral environments.

Summarizing, the oxygen net, one of the $BaCeO_3$ perovskite derivatives, defines a complex allocation matrix for the structural protons. This allows one to hypothesize the existence of an extended conformational space, defining the proton placement in the X:$BaCeO_3$ material bulk: the former will be investigated in a following work. However, it is already possible to hypothesize that preferred placements on the oxygen site in the octahedral arrangement—in the order: $InO_6 > CeO_6 > YO_6$—as well as preferential interoctahedral diffusion way—in the order: $YO_6 \rightarrow CeO_6 > CeO_6 \rightarrow CeO_6 > InO_6 \rightarrow CeO_6$—can prevail for protons belonging to $BaCeO_3$ perovskite derivatives. The preferential placement behavior here proposed is in agreement with that, reproducing the experimental trend, already found by Björketun et al.[28] And, on the whole, our results also confirm the unifying view[28] for which both the association of the protons with discrete sites[25] and the basicity[27] of the same sites play a basis role in the conductivity phenomena.

Final considerations deserve the unmixing phenomena characterizing the Y:$BaCeO_3$ materials.[21] Figure 4 reports the ρ *vs.* ε plot of the Y2:$Ba_8Ce_{25}O_{62}$ fragment. The main characteristics concern the presence of two broad bands in the ranges, from −40 to −35 eV and −28 to −10 eV, respectively, and the shift to lower energy values of the bands that we attributed to effects produced by the barium AOs. In fact, the two broad bands have the same properties—specifically a large mix of Ba, O, and Y AOs—of the band centered at ∼− 10 eV already found when considering the monodoped Y fragment. More interestingly, a remarkable contribution of the lateral Y atom is also found in these bands. Of course, a symmetric behavior, here not shown, of the central Y AOs is observed on the MOs formed by yttrium, barium, and oxygen atoms defining the lateral Y atom environment. These interactions, in presence of high percentage of yttrium atoms in barium cerate matrices, reinforce the structural instability mentioned above and could be straightforwardly related to the occurrence of YO_6 moieties' clustering, which could induce the experimentally observed unmixing phenomena

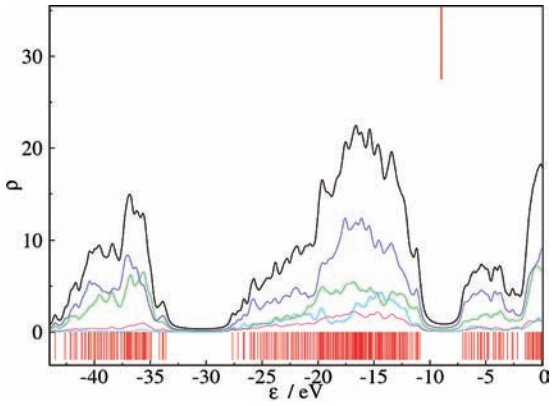

Figure 4. C-SPA/P-DOS analysis of the Y_2:$Ba_8Ce_{25}O_{62}$ fragment treated by the Y-2 approach: orbital contribution of atomic sets, included in the $Ba_8Y_2O_6$ moiety (Ba_8 group: green line; central Y atom: blue line; lateral Y atom: cyan line; central octahedron O_6 group: purple line; central Ba_8YO_6 moiety: black line), to the Ba_8YO_6 (central moiety) MOs against energy values, ρ *vs*. ε. The red bars individuate the *i* eigenstates of the whole Y_2:$Ba_8Ce_{25}O_{62}$ fragment. The ρ lines are obtained by a convolution of fixed-width Lorentzian curves centered on the energy bin used in the DOS analysis, with the height proportional to the weight of the AO set contribution in the bin. The red line on the top shows the border between HOMO and LUMO.

of the Y:$BaCeO_3$ derivatives, with production of yttrium and barium oxide species.[21]

Conclusions

The size of the suggested fragment was shown to be a good compromise between the physical consistency of the calculated model results and the computational resources employed to get them. The computational findings concerning the same compounds belonging to the *Pmcn* and *I2/m* space groups would seem to point to a better agreement of the former with the experimental results. As a consequence, the incoming study on the proton diffusion occurring in the title conductors' models, at the beginning, will be mainly related to derivatives belonging to the former space group.

However, it is straightforward that the QC cluster approach here proposed, even considering large fragments, is not specifically addressable to discriminate among the space groups inferable for a given material. Nevertheless, the local description of significant geometrical characteristics, namely distances and angles, are easily captured also by lower level ECP basis sets in the frame of the HF paradigm. Concerning this, our approach allowed us to suggest a possible origin of the bimodal Y−O distance distribution recently found by EXAFS experiments on Y-doped $BaCeO_3$ materials. Of course, it is possible to fall into the analysis of materials, like the In:$BaCeO_3$ derivatives, which require care in the choice of the basis sets in order to get structure results in better agreement with the experimental ones.

The use of the ONIOM approach, at least in the formulation here considered, seems to be discouraged. On the contrary, the C-SPA/P-DOS analysis and the *M-ca* procedure, considered together, would seem able to rationalize both structural and conducting properties of the doped sites in the $BaCeO_3$ derivatives, on pure electronic basis. In particular: (i) in order to increase the material conductivity, a dopant species has to leave unchanged, or even decrease, the local basicity of the oxygen octahedral environment, while (ii) small structural changes, not affecting the basicity properties above, seem to be less effective in producing conductivity modifications. After these findings, which are in general agreement with the current views, we intend to extend the here-considered protocol—i.e., the QC cluster approach followed by electronic analysis procedures—to different systems in which structural protons as well as new basis materials, e.g., $BaZrO_3$, and dopant species, e.g., Gd, will be considered. Hopefully, these further applications could confirm the present conclusions and accordingly could help to develop predictive tools helpful in studying solid conducting materials.

Acknowledgment. The authors are grateful to Dr. Francesco Ferrante for supplying the homemade C-SPA/P-DOS code and for giving critical suggestions along the investigation of the electronic population analysis. A.C. thankfully acknowledges the tutoring activity of Prof. Antonio Emanuele with respect to his Ph.D. fellowship project. Financial support has been provided by the Italian Ministero dell'Università e della Ricerca (PRIN 2006: *Ceramici Protonici per Celle a Combustibile*) and by the Università di Palermo (ex 60%: *Ossidi Misti a Base di Cerato di Bario: Sintesi, Caratterizzazione Strutturale e Studio Computazionale del Meccanismo di Conduzione Protonica*).

References and Notes

(1) Iwahara, H. *Solid State Ionics* **1995**, *77*, 289–298.
(2) Bonanos, N.; Knight, K. S.; Ellis, B. *Solid State Ion.* **1995**, *79*, 161–170.
(3) Kreuer, K. D. *Annu. Rev. Mater. Res.* **2003**, *33*, 333–359.
(4) Tomita, A.; Hibino, T.; Suzuki, M.; Sano, M. *J. Mater. Sci.* **2004**, *39*, 2493–2497.
(5) Iwahara, H.; Asakura, Y.; Katahira, K.; Tanaka, M. *Solid State Ionics* **2004**, *168*, 299–310.
(6) Song, C. *Catal. Today* **2002**, *77*, 17–49.
(7) Islam, M. S. *J. Mater. Chem.* **2000**, *10*, 1027–1038.
(8) Wakamura, K. *J. Phys. Chem. Solids* **2005**, *66*, 133–142.
(9) Kreuer, K. D. *Chem. Mater.* **1996**, *8*, 610–641.
(10) Kreuer, K. D.; Fuchs, A.; Maier, J. *Solid State Ionics* **1995**, *77*, 157–162.
(11) Knight, K. S.; Bonanos, N. *Solid State Ionics* **1995**, *77*, 189–194.
(12) Knight, K. S.; Bonanos, N. *Mater. Res. Bull.* **1995**, *30*, 347–356.
(13) Knight, K. S.; Soar, M.; Bonanos, N. *J. Mater. Chem.* **1992**, *2*, 709–712.
(14) Melekh, B. T.; Egorov, V. M.; Baikov, Y. M.; Kartenko, N. F.; Filin, Y. N.; Kompan, M. E.; Novak, I. I.; Venus, G. B.; Kulik, V. B. *Solid State Ionics* **1997**, *97*, 465–470.
(15) (a) Scherban, T.; Villeneuve, R.; Abello, L.; Lucazeau, G. *Solid State Ionics* **1993**, *61*, 93–98. (b) Scherban, T.; Villeneuve, R.; Abello, L.; Lucazeau, G. *J. Raman Spectrosc.* **1993**, *24*, 805–814.
(16) Knight, K. S. *Solid State Ionics* **1994**, *74*, 109–117.
(17) Glazer, A. M. *Acta Crystallogr. A* **1975**, *31*, 756–762.
(18) Knight, K. S. *Solid State Ionics* **2000**, *127*, 43–48.
(19) Takeuchi, K.; Loong, C. K.; Richardson Jr., J. W.; Guan, J.; Dorris, S. E.; Balachandran, U. *Solid State Ionics* **2000**, *138*, 63–77.
(20) Malavasi, L.; Ritter, C.; Chiodelli, G. *Chem. Mater.* **2008**, *20*, 2343–2351.
(21) Longo, A.; Giannici, F.; Balerna, A.; Ingrao, C.; Deganello, F.; Martorana, A. *Chem. Mater.* **2006**, *18*, 5782–5788.
(22) Giannici, F.; Longo, A.; Deganello, F.; Balerna, A.; Aricò, A. S.; Martorana, A. *Solid State Ionics* **2007**, *178*, 587–591.
(23) Giannici, F.; Longo, A.; Balerna, A.; Kreuer, K. D.; Martorana, A. *Chem. Mater.* **2007**, *19*, 5714–5720.
(24) Giannici, F.; Longo, A.; Balerna, A.; Deganello, F.; Martorana, A. *Chem. Mater.*, accepted for publication.
(25) Hempelmann, R.; Karmonik, C.; Matzke, T.; Cappadonia, M.; Stimming, U.; Springer, T.; Adams, M. A. *Solid State Ionics* **1995**, *77*, 152–156.
(26) Kreuer, K.-D. *Solid State Ionics* **2001**, *145*, 295–306.
(27) Kreuer, K.-D.; Münch, W.; Ise, M.; He, T.; Fuchs, A.; Traub, U.; Maier, J. *Ber. Bunsen-Ges. Phys. Chem.* **1997**, *101*, 1344–1350.
(28) (a) Björketun, M. E.; Sundell, P. G.; Wahnström, G. *Phys. Rev. B* **2007**, *76*, 54307–54315. (b) Sundell, P. G.; Björketun, M. E.; Wahnström, G. *Phys. Rev. B* **2007**, *73*, 104112(1−10). (c) Björketun, M. E.; Sundell, P. G.; Wahnström, G. *Faraday Discuss.* **2007**, *134*, 247–265.
(29) Glockner, R.; Islam, M. S.; Norby, T. *Solid State Ionics* **1999**, *122*, 145–156.
(30) Wu, J.; Davies, R. A.; Islam, M. S.; Haile, S. M. *Chem. Mater.* **2005**, *17*, 846–851.

(31) (a) Davies, R. A.; Islam, M. S.; Chadwick, A. V.; Rush, G. E. *Solid State Ion.* **2000**, *130*, 115–122. (b) Islam, M. S.; Davies, R. A.; Gale, J. D. *Chem. Mater.* **2001**, *13*, 2049–2055.

(32) Islam, M. S.; Davies, R. A.; Fisher, C. A. J.; Chadwick, A. V. *Solid State Ion.* **2001**, *145*, 333–338.

(33) Islam, M. S. *Solid State Ionics* **2002**, *154*−*155*, 75–85.

(34) Cherry, M.; Islam, M. S.; Gale, J. D.; Catlow, C. R. A. *J. Phys. Chem.* **1995**, *99*, 14614–14618.

(35) Munch, W.; Seifert, G.; Kreuer, K. D.; Maier, J. *Solid State Ionics* **1996**, *86*−*88*, 647–652.

(36) Munch, W.; Kreuer, K. D.; Seifert, G.; Maier, J. *Solid State Ionics* **2000**, *136*−*137*, 183–189.

(37) Scherban, T.; Villeneuve, R.; Abello, L.; Lucazeau, G. *Solid State Commun.* **1992**, *84*, 341–344.

(38) Matthew, N. *J. Catal.* **2003**, *216*, 73–88, and reference therein.

(39) Mulliken, R. S. *J. Chem. Phys.* **1955**, *23*, 1833–1840.

(40) Foresman, J. B.; Frisch, Æ. *Exploring Chemistry with Electronic Structure Methods*, 2nd ed.; Gaussian Inc.: Pittsburgh PA, 1996.

(41) Levine, N. I. *Quantum Chemistry*, 5th ed.; Prentice Hall: Upper Saddle River NJ, 1999.

(42) Duca, D.; Ferrante, F.; La Manna, G. *J. Phys. Chem. C* **2007**, *111*, 5402–5408.

(43) Ros, P.; Schuit, G. C. A. *Theor. Chim. Acta* **1966**, *4*, 1–12.

(44) Cammarata, A. In *Science and Supercomputing in Europe, HPC-Europa Transnational Access Report*: 2007; Alberigo, P., Erbacci, G., Garofalo, F., Monfardini, S., Eds; Casalecchio di Reno: Bononia,2007Chapter, Computational Studies of the Structure and of the Proton Transport Phenomena in Systems Derived from Barium Cerate Perovskite Structure, pp119−129.

(45) Barone, G.; Casella, G.; Giuffrida, S.; Duca, D. *J. Phys. Chem. C* **2007**, *111*, 13033–13043.

(46) Armata, N.; Baldissin, G.; Barone, G.; Cortese, R.; D'Anna, V.; Ferrante, F.; Giuffrida, S.; Li Manni, G.; Prestianni, A.; Rubino, T.; Duca, D. *Top. Catal.* **2009**, . in press.

(47) Frisch, M. J.; Trucks, G. W.; Schlegel, H. B.; Scuseria, G. E.; Robb, M. A.; Cheeseman, J. R.; Montgomery Jr., J. A.; Vreven, T.; Kudin, K. N.; Burant, J. C.; Millam, J. M.; Iyengar, S. S.; Tomasi, J.; Barone, V.; Mennucci, B.; Cossi, M.; Scalmani, G.; Rega, N.; Petersson, G. A.; Nakatsuji, H.; Hada, M.; Ehara, M.; Toyota, K.; Fukuda, R.; Hasegawa, J.; Ishida, M.; Nakajima, T.; Honda, Y.; Kitao, O.; Nakai, H.; Klene, M.; Li, X.; Knox, J. E.; Hratchian, H. P.; Cross, J. B.; Bakken, V.; Adamo, C.; Jaramillo, J.; Gomperts, R.; Stratmann, R. E.; Yazyev, O.; Austin, A. J.; Cammi, R.; Pomelli, C.; Ochterski, J. W.; Ayala, P. Y.; Morokuma, K.; Voth, G. A.; Salvador, P.; Dannenberg, J. J.; Zakrzewski, V. G.; Dapprich, S.; Daniels, A. D.; Strain, M. C.; Farkas, O.; Malick, D. K.; Rabuck, A. D.; Raghavachari, K.; Foresman, J. B.; Ortiz, J. V.; Cui, Q.; Baboul, A. G.; Clifford, S.; Cioslowski, J.; Stefanov, B. B.; Liu, G.; Liashenko, A.; Piskorz, P.; Komáromi, I.; Martin, R. L.; Fox, D. J.; Keith, T.; Al-Laham, M. A.; Peng, C. Y.; Nanayakkara, A.; Challacombe, M.; Gill, P. M. W.; Johnson, B.; Chen, W.; Wong, M. W.; Gonzalez, C.; Pople, J. A. *Gaussian 03, Revision D.02*; Gaussian, Inc.: Wallingford CT, 2005.

(48) (a) Becke, A. D. *J. Chem. Phys.* **1993**, *98*, 5648–5652. (b) Stephens, P. J.; Devlin, J. F.; Chabalowsky, C. F.; Frisch, M. J. *J. Phys. Chem.* **1994**, *98*, 11623–11627.

(49) (a) Svensson, M.; Humbel, S.; Froese, R. D. J.; Matsubara, T.; Sieber, S.; Morokuma, K. *J. Phys. Chem.* **1996**, *100*, 19357–19363. (b) Dapprich, S.; Komàroni, I.; Byun, K. S.; Morokuma, K.; Frisch, M. J. *J. Mol. Struct. (Theochem)* **1999**, *461*−*462*, 1–21.

(50) Bacskay, G. B. *Chem. Phys.* **1981**, *61*, 385–404.

(51) (a) Hariharan, P. C.; Pople, J. A. *Theor. Chem. Acc.* **1973**, *28*, 213–222. (b) Francl, M. M.; Petro, W. J.; Hehre, W. J.; Binkley, J. S.; Gordon, M. S.; De Frees, D. J.; Pople, J. A. *Theor. Chem. Acc.* **1982**, *77*, 3654.

(52) (a) Binkley, J. S.; Pople, J. A.; Hehre, W. J. *J. Am. Chem. Soc.* **1980**, *102*, 939–947. (b) Gordon, M. S.; Binkley, J. S.; Pople, J. A.; Pietro, W. J.; Hehre, W. J. *J. Am. Chem. Soc.* **1982**, *104*, 2797–2803. (c) Pietro, W. J.; Francl, M. M.; Hehre, W. J.; Defrees, D. J.; Pople, J. A.; Binkley, J. S. *J. Am. Chem. Soc.* **1982**, *104*, 5039–5048. (d) Dobbs, K. D.; Hehre, W. J. *J. Comput. Chem.* **1986**, *7*, 359–378. (e) Dobbs, K. D.; Hehre, W. J. *J. Comput. Chem.* **1987**, *8*, 861–879.

(53) (a) Cundari, T. R.; Stevens, W. J. *J. Chem. Phys.* **1993**, *98*, 5555–5565. (b) Stevens, W. J.; Krauss, M.; Basch, H.; Jasien, P. G. *Can. J. Chem.* **1992**, *70*, 612–630.

(54) (a) Pacios, L. F.; Christiansen, P. A. *J. Chem. Phys.* **1985**, *82*, 2664–2671. (b) Hurley, M. M.; Pacios, L. F.; Christiansen, P. A.; Ross, R. B.; Ermler, W. C. *J. Chem. Phys.* **1986**, *84*, 6840–6853. (c) LaJohn, L. A.; Christiansen, P. A.; Ross, R. B.; Atashroo, T.; Ermler, W. C. *J. Chem. Phys.* **1987**, *87*, 2812–2824. (d) Ross, R. B.; Powers, J. M.; Atashroo, T.; Ermler, W. C.; LaJohn, L. A.; Christiansen, P. A. *J. Chem. Phys.* **1990**, *93*, 6654–6559.

(55) (a) Dolg, M.; Wedig, U.; Stoll, H.; Preuss, H. *J. Chem. Phys.* **1987**, *86*, 866–872. (b) Kaupp, M.; von Schleyer, P. R.; Stoll, H.; Preuss, H. *J. Chem. Phys.* **1991**, *94*, 1360–1366. (c) Dolg, M.; Stoll, H.; Preuss, H.; Pitzer, R. M. *J. Phys. Chem.* **1993**, *97*, 5852–5859.

(56) Peterson, K. A. *J. Chem. Phys.* **2005**, *119*, 11099–11112.

(57) (a) Feller, D. *J. Comput. Chem.* **1996**, *17* (13), 1571–1586. (b) Schuchardt, K. L.; Didier, B. T.; Elsethagen, T.; Sun, L.; Gurumoorthi, V.; Chase, J.; Li, J.; Windus, T. L. *J. Chem. Inf. Model.* **2007**, *47* (3), 1045–1052.

(58) The differences in the reported average charge values were obtained considering the CRENBL optimization performed on the different Ξ:$Ba_8Ce_{26}O_{62}$ fragments, but they are actually unchanged, considering the relative values of the yttrium and indium derivatives, when the results obtained by the CS1 and CVP are considered.

JP901074P